Int J Adv Manuf Technol (2017) 92:3167–3185
DOI 10.1007/s00170-017-0357-3

ORIGINAL ARTICLE

A unified analytical cutting force model for variable helix end mills

Ding Chen[1] · **Xiaojian Zhang**[1] · **Yakun Xie**[1] · **Xiaoming Zhang**[1] · **Han Ding**[1]

Received: 30 November 2016 / Accepted: 28 March 2017 / Published online: 19 April 2017

Abstract The paper proposes a unified analytical cutting force model based on a predictive machining theory for variable helix end mill considering cutter runout. The variable helix end mill is divided into a set of differential oblique elements along the axial direction. The cutting process of oblique element is based on the non-equidistant shear zone model and the equivalent plane method. The cutting forces of oblique element are modeled by shearing force components due to shearing at the shear zone and edge force components due to rubbing in the tertiary zone. In the primary shear zone, a modified Johnson-Cook model is introduced to account for the material size effect affected by varying instantaneous uncut chip thickness (IUCT) during milling process. In the tertiary zone, edge radius and the partial effective rake angle are included in the analytical model in order to take into account the rubbing effect precisely. The total instantaneous cutting forces are obtained by summing up the cutting forces acting oblique elements on all flutes. The unified analytical cutting force model is verified by experimental data using four different types of end mills, and a good agreement of the predicted and measured cutting forces shows that the proposed model is valid for variable helix end mills.

Keywords Variable helix · End mill · Cutting force · Oblique cutting · Cutter runout

✉ Xiaojian Zhang
xjzhang@hust.edu.cn

[1] Mechanical Engineering, Huazhong University of Science & Technology, 1037 Luoyu Load, Wuhan 430074, China

Nomenclature

$\phi_{i,j}(t)$	Angular position of the jth axial oblique element of the ith flute
ϕ_{pi}	Pitch angle between the flute number i and the flute number $i-1$ at the tip of end mill
N	The number of flutes of the end mill
$\phi_0(t)$	Angle position of the reference cutting edge $i=1$ with axial elevation $z=0$ at time t
ϕ_0	Initial angular position of the reference cutting edge
n	Spindle speed
$\psi_{i,j}$	Radial lag angle of the jth axial oblique element of the ith flute
β_i	The ith helix angle of end mill
R	The radius of end mill
f_z	The normal feed per tooth
$\phi_{pi,j}$	Pitch angle of jth oblique element between ith flute and $(j-1)$th flute
K_{tc}, K_{rc}, K_{ac}	Tangential, radial, and axial shearing force coefficients
K_{te}, K_{re}, K_{ae}	Tangential, radial, and axial edge force coefficients
$h_{i,j}(t)$	The instantaneous uncut cut thickness
m_i	Index number denoting that the current tooth i is to remove the materials left by its m_ith previous tooth
$R_{i,j}$	The actual effective radius of the cutting edge
ρ,λ	Runout amplitude and runout angle
$V_{i,j}$	The peripheral cutting velocity of end mill
ϕ_{en},ϕ_{ex}	Entry angle and exit angle

α_n, α_r	The normal rake angle and radial rake angle
λ_s	Edge inclination angle
η_e	Equivalent plane angle
η_{sh}	The shear flow angle
η_c	The chip flow angle
a_r, a_p	Radial depth of cut and axial depth of cut
k	The unequal portion in the primary shear zone
χ	Taylor-Quinney coefficient
ρ_m, C_p, k_p	Material density, heat capacity and heat conductivity coefficient
φ_n	The normal shear angle
β_n	The normal friction angle in rake face
C_1,C_2	Empirical machining constants
$\gamma, \dot{\gamma}, \dot{\gamma}_m, \dot{\gamma}_0$	Shear strain, strain rate, maximum strain rate in shear face, and the reference shear strain rate
A, B, C, m, n	Coefficients of the Johnson-Cook model
T, T_r, T_m	Material temperature, room temperature, and material melting temperature
τ_s	Shear flow stress
α_c,u	Empirical constant and exponential factor
G	The shear modulus of workpiece
b_g	The magnitude of the Burgess vector
η	The strain gradient
L	The length of the primary shear zone
h	Uncut chip thickness
$h_{\lim}$	The limiting value of instantaneous uncut cut thickness
r_e	The edge radius
α_{ref}	The partial effective rake angle

1 Introduction

Milling process is one of the most widely used machining processes for aeronautical, aerospace, die/mold, and automobile components. Many undesired issues such as cutter wear, cutter breakage, chatter regeneration, and surface quality are greatly dependent on the cutting forces, whose prediction is affected by the geometry of tool and workpiece, especially when the tool has a complex geometry in realistic industrial machining processes. For this reason, the precise prediction of cutting forces of variable helix end mills is very necessary for the analysis and optimization of milling machining performance.

Literature review [1] reveals that the prediction method of cutting forces can be roughly classified as mechanistic and analytical approaches. The prediction of cutting forces in mechanistic model depends heavily on the cutting force coefficients, usually as average cutting force coefficients or instantaneous cutting force coefficients, which are calibrated via a large number of cutting experiments. Tlusty and MacNeil [2] calculated the discrete cutting forces in milling process with the average milling force coefficients. Kline and DeVor [3] developed a model including cutter runout for predicting cutting forces with the average cutting force coefficients in end milling. Gradišek et al. [4] predicted the cutting forces for a general end mill with the average cutting force coefficients, which are identified by a series of slot-milling experiments and the average cutting force model. For predicting the cutting forces more accurately, Wan et al. [5] developed a new cutting force prediction approach for general end mills using the instantaneous cutting force coefficients expressed as exponential functions of the varied instantaneous uncut cut thickness. Besides, there are some other methods for identification of cutting force coefficients. Gonzalo et al. [6] and Adetoro and Wen [7] have used the finite element method to evaluate both the average and instantaneous cutting force coefficients. Adem et al. [8] proposed an optimization technique method for identifying the cutting force coefficients in the linear and non-linear force models.

Despite the simple structure of the mechanistic models, their predictive capability is only valid for a known cutter profile and tool/workpiece material combination. The cutting force coefficients need to be identified once again when the cutter profile or the material combination changes. Moreover, the determination of cutting force coefficients depends heavily on amounts of experimental database. Actually, the analytical cutting force model is an alternative method to predict cutting forces. It describes a mathematical relationship between the cutting forces and the mechanical parameters, based on the theory of orthogonal or oblique cutting mechanics [9], which can be used for calculation of cutting force coefficients. Hence, this approach is independent of the repeated experimental calibration and can be applied to the complex milling process. Oxley and Young [10] devoted great effort into the investigation of an analytical approach to assess machinability and developed a predictive machining theory. Li et al. [11] proposed a cutting force model in helical end milling process based on Oxley's predictive machining theory, in

which the machining characteristic factors are obtained from input data of cutting conditions, tool geometry, and workpiece material properties. Later, Lalwani et al. [12] have presented extension of Oxley's predictive machining theory with the Johnson and Cook flow stress model, which considers the effects of strain hardening, strain rate sensitivity, and thermal softening on the chip formation. With the Johnson and Cook flow stress model, the analytical model is also able to predict the temperatures and stresses at primary deformation zone and chip-tool contact zone. Recently, Moufki et al. [13] applied the thermomechanical model of oblique cutting to calculate the milling forces by means of the material thermomechanical characteristics and tool-chip interface friction coefficient as input parameters. Fu et al. [14] also presented an analytical force model with cutter runout for ball-end milling based on a predictive machining theory.

In all the work mentioned earlier, it is noticed that the structure of milling cutters is equal helix angle. Actually, the variable helix cutter can be used to reduce the forced vibration, obtain the better surface machining quality, enhance the durability of tool, and improve the production efficiency [15, 16]. Compared with the mechanistic force model, the analytical force model has several advantages: firstly, avoidance of laborious experimental calibration; secondly, it can be used to investigate the effects of cutter geometry or machining parameters on the cutting forces, especially for the variable helix cutter. In order to achieve high accuracy and high efficiency in cutting, it is necessary to establish the analytical cutting force model for designing variable helix end mill. In the present work, a unified analytical cutting force model for variable helix end mill is proposed. The instantaneous uncut chip thickness (IUCT) varies distinctly for variable helix end mill, especially due to the existence of cutter runout. Therefore, cutter runout is considered in the modeling of variable helix end tool milling process. During the milling modeling process, the shear flow stress in the primary shear zone is estimated by introducing a modified Johnson-Cook material constitutive law, which takes into account the work hardening, temperature softening, and material strengthening. To calculate the rubbing effect precisely, edge radius and the partial effective rake angle involved in the edge force prediction are included in the analytical model. Then, the milling tests are carried out with different types of end mills to verify the validity of the proposed model. Finally, the effects of tool geometries and milling parameters on cutting forces are revealed through numerical simulations.

The organization of this paper is as follows: the geometry of the variable end mill, the IUCT with cutter runout, and the related parameters in end milling process are introduced in Sect. 2. The modeling of non-equal shear zone oblique cutting and the estimation of shear stress in primary deformation zone are included in Sect. 3. Subsequently, Sect. 4 investigated the shearing force coefficients in primary shear zone and edge force coefficients in tertiary zone. In Sect. 5, four types of end mills are implemented to evaluate the effectiveness of the unified analytical model. Effects of tool geometries and milling parameters on cutting forces are discussed in Sect. 6. Finally, some important conclusions are given in Sect. 7.

2 Theoretical model of the milling process

2.1 Geometric model of the variable helix end mill

In this section, the end milling operation is analyzed with respect to the global Cartesian coordinate system (*O-XYZ*). The detailed geometry of a three-fluted variable helix end mill is shown in Fig. 1. The geometric center of end mill is set on the origin *O*. *X*-axis is along the negative feed direction, *Y*-axis is perpendicular to the machined surface, and *Z*-axis is aligned with the tool axis direction. For the sake of convenience, the variable helix end mill is divided into a finite number of differential oblique elements along the axial direction. For an oblique element of thickness dz at axial elevation z, the modeling process is as follows.

The angular position $\phi_{i,j}(t)$ of the jth axial oblique element of the ith flute (element P in Fig. 1), which is measured clockwise from the positive *Y*-axis, is characterized as the function of the rotation angle $\phi_0(t)$, the pitch angle ϕ_{pi}, and the radial lag angle $\psi_{i,j}$, and it can be expressed as

$$\phi_{i,j}(t) = \begin{cases} \phi_0(t) - \psi_{i,j} & (i = 1) \\ \phi_0(t) + \sum_{i=2}^{N_i} \phi_{pi} - \psi_{i,j} & (1 < i = N_i \leq N) \end{cases} \quad (1)$$

where N is the number of flutes of the end mill. ϕ_{pi} denotes the pitch angle between the flute number i and the flute number $i - 1$ at the bottom surface of end mill. The previous formulation allows the pitch angle to vary among different flutes for variable pitch angle end mill. $\phi_0(t)$ indicates the cutter angular position of the reference cutting edge $i = 1$ with axial elevation $z = 0$ at time t.

$$\phi_0(t) = 2\pi nt/60 + \phi_0 \quad (2)$$

where n is the spindle speed (r/min) and ϕ_0 is the cutter initial angular position of the reference cutting edge.

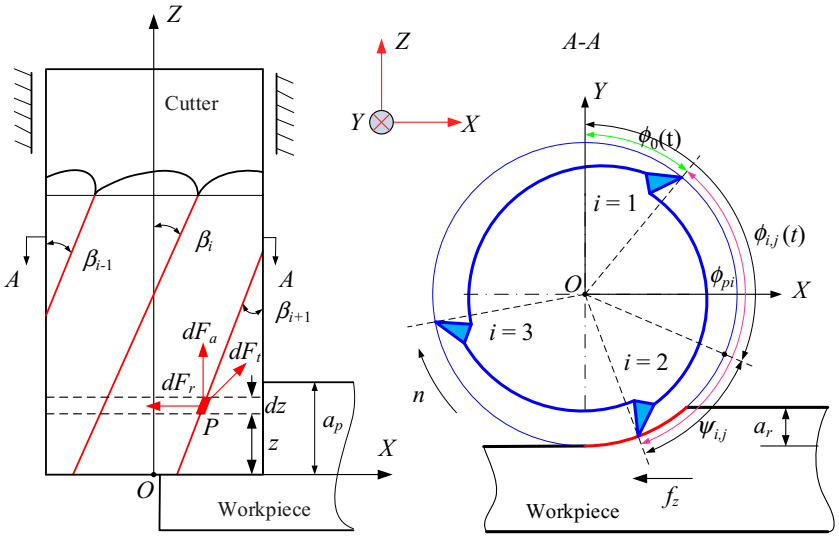

Fig. 1 Geometric model of the variable helix end mill

It is evident that the angular position at axial elevation z lags behind the angular position at the tip of end mill due to the local helix angle $\beta_{i,j}$ and the periphery radius R. Then, the radial lag angle $\psi_{i,j}$ can be expressed as

$$\begin{cases} \beta_{i,j} = \beta_i \\ \psi_{i,j} = j \cdot dz \dfrac{\tan\beta_{i,j}}{R} \end{cases} \tag{3}$$

The feed per tooth of every oblique element for a variable pitch and variable helix end mill is no longer a constant but varies from tooth to tooth as function of the number of teeth N, the normal feed per tooth f_z, and the variable pitch angle $\phi_{pi,j}$. The feed per tooth of the jth axial element of the ith flute is described by

$$f_{i,j} = N f_z \cdot \frac{\phi_{pi,j}}{2\pi} \tag{4}$$

where $\phi_{pi,j}$ means the pitch angle of the jth oblique element between the flute number i and the flute number $i-1$ along axial direction, which is defined as

$$\phi_{pi,j} = \begin{cases} 2\pi + \phi_{1,j}(t) - \phi_{N,j}(t) = \phi_{p1} - j \cdot dz \dfrac{\tan\beta_{1,j} - \tan\beta_{N,j}}{R} & (i = 1) \\ \phi_{i,j}(t) - \phi_{i-1,j}(t) = \phi_{pi} - j \cdot dz \dfrac{\tan\beta_{i,j} - \tan\beta_{i-1,j}}{R} & (1 < i \le N) \end{cases} \tag{5}$$

2.2 End-milling cutting force modeling

During the chip formation, both the shearing action of the primary shear zone and the rubbing effect of the tertiary deformation zone exist. The cutting force components are usually expressed as a superposition of shearing force and rubbing force.

$$\begin{cases} dF_{i,j,t} = \left[K_{tc} h_{i,j}(t) + K_{te}\right] \cdot dz \\ dF_{i,j,r} = \left[K_{rc} h_{i,j}(t) + K_{re}\right] \cdot dz \\ dF_{i,j,a} = \left[K_{ac} h_{i,j}(t) + K_{ae}\right] \cdot dz \end{cases} \tag{6}$$

where $h_{i,j}(t)$ represents the IUCT with cutter runout (Sect. 2.3). K_{tc}, K_{rc}, and K_{ac} are the shearing force coefficients in tangential, radial, and axial direction, respectively (Sect. 4.1); K_{te}, K_{re}, and K_{ae} are the edge force coefficients in tangential, radial, and axial direction, respectively (Sect. 4.2).

Once the three cutting force components of the jth oblique element of the ith flute are obtained, they can be mapped along the X, Y, and Z directions using the following matrix transition in Eq. (7).

$$\begin{bmatrix} dF_{i,j,x} \\ dF_{i,j,y} \\ dF_{i,j,z} \end{bmatrix} = g\left(\phi_{i,j}(t)\right) \begin{bmatrix} -\cos\phi_{i,j} & -\sin\phi_{i,j} & 0 \\ \sin\phi_{i,j} & -\cos\phi_{i,j} & 0 \\ 0 & 0 & 1 \end{bmatrix} \cdot \begin{bmatrix} dF_{i,j,t} \\ dF_{i,j,r} \\ dF_{i,j,a} \end{bmatrix} \tag{7}$$

where $g(\phi_{i,j}(t))$ is the window function. It equals one if the cutting edge is engaged with the workpiece or equals zero.

Then, the cutting forces acting on a flute at a particular instant $F_{i,q}(t)$ are obtained by numerically integrating the cutting forces acting on each oblique element. Subsequently, the total cutting forces $F_q(t)$ exerted on the tool at a given time are determined by summing the forces acting on all of the flutes.

$$\begin{cases} F_{i,q}(t) = \sum_j dF_{i,j,q}\left(\phi_{i,j}(t)\right) \\ F_q(t) = \sum_{i=1}^{N} F_{i,q}(t), \quad q = X, Y, Z \end{cases} \tag{8}$$

2.3 IUCT with cutter runout

The precise calculation of the IUCT is essential for the accurate prediction of cutting forces in the machining process. IUCT is defined as the radial distance between the current cutting circular path and the previous cutting circular path. Actually, the axis of the spindle does not coincide with the axis of the end mill as the tool machine manufacture and setup errors exist. Thus, the cutter runout is commonly encountered in multi-fluted milling progress with rotary cutting tools. The cutter runout contains the axis tilt and the radial cutter runout two parts. They can be characterized by four parameters: offset distance ρ, offset location angle λ, cutter tilt angle τ, and cutter tilt location angle ϕ. Compared with three different types of cutter runout models, Wan et al. [17] found that the radial runout model has relatively simple runout parameters and good prediction accuracy. Therefore, only the radial runout model is considered in this work.

The detailed procedure of tooth path trajectories with cutter runout in machine process is illustrated in Fig. 2. O and O' represent the spindle rotational center and actual cutter geometrical center, respectively. The runout amplitude ρ is defined as the distance $\overline{OO'}$. The runout angle λ measured in clockwise denotes the angle between the direction $\overline{OO'}$ and the nearest cutting edge. The presence of cutter runout will shift the cutting circular path from theoretical position. Therefore, the IUCT of each point of the cutting edge will be redistributed. Due to the effect of the cutter runout, candidates of the IUCT $h^c_{i,j}(t)$ will be calculated as

$$h^c_{i,j}(t) = \sum_{1}^{m_i} f_{i,j}\cdot\sin\phi_{i,j}(t) + R_{i,j} - R_{i-m_i,j} \tag{9}$$

where m_i is an index number denoting that the current tooth i is removing the material left by the previous m_i tooth.

From the geometrical relation in Fig. 2, the effective radius of the cutting edge depending on cutter runout parameters can be obtained by

$$R_{i,j} = \begin{cases} R + \rho\cos\left(\lambda - \psi_{i,j}\right) & (i = 1) \\ R + \rho\cos\left(\lambda - \psi_{i,j} - \sum_{i=2}^{N_i}\phi_{pi}\right) & (1 < i = N_i \le N) \end{cases} \tag{10}$$

where $R_{i,j}$ and R represent the actual and ideal periphery radii of the ith cutting edge, respectively. Then, the peripheral cutting velocity depending on the effective radius of the cutting edge is calculated as

$$V_{i,j} = 2\pi n\cdot R_{i,j} \tag{11}$$

As seen from the right part of Fig. 2, each tooth is probably the cutting material left by any one of the previous N tooth. Therefore, there are N candidates of the IUCT for an N-flute end mill. The actual IUCT is the minimum value among N candidates. In addition, the final IUCT should not be a negative value.

$$h_{i,j}(t) = \max\left(\min\left(h^c_{1,j}(t), h^c_{2,j}(t), \ldots, h^c_{N,j}(t)\right), 0\right) \tag{12}$$

The radial entry angle and exit angle are key parameters for the accurate prediction of cutting forces. If ϕ_{en} is the angle at which the cutter enters the cutting zone, ϕ_{ex} is the angle at which the cutter exits the cutting zone. Then, the radial entry angle and exit angle are determined by the following equation:

$$\begin{cases} \phi_{en} = 0 \quad \text{and} \quad \phi_{ex} = \cos^{-1}(1 - a_r/R) & \text{for up-milling} \\ \phi_{en} = \pi - \cos^{-1}(1 - a_r/R) \quad \text{and} \quad \phi_{ex} = \pi & \text{for down-milling} \end{cases} \tag{13}$$

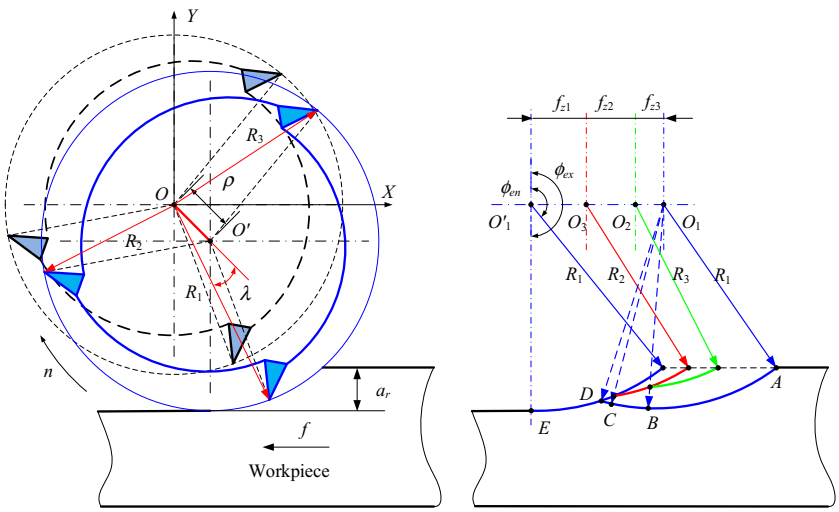

Fig. 2 Cutter runout and tooth path trajectories

3 Modeling of oblique cutting

3.1 Non-equal shear zone oblique cutting

The mechanics of oblique cutting is analyzed based on the normal cutting plane method or the equivalent plane method. The mechanics of oblique cutting is regarded as a two-dimensional cutting process in the equivalent plane method. Therefore, the equivalent plane method is briefly introduced. For the convenience of study, six planes (the reference plane P_r, the equivalent plane P_e, the cutting plane P_s, the normal plane P_n, the shear plane P_{sh}, and the rake plane A_r) are introduced in oblique cutting process, as shown in Fig. 3. According to the geometric relationship in oblique cutting, some essential parameters for the analysis in the machining process are summarized as follows [18].

The normal rake angle α_n measured in the normal plane P_n is obtained from the radial rake angle α_r and edge inclination angle λ_s all along the cutting edge. The edge inclination angle is equal to the local helix angle $\beta_{i,j}$ during modeling of oblique cutting.

$$\alpha_n = \tan^{-1}\left(\tan\alpha_r \cos\beta_{i,j}\right) \tag{14}$$

Equivalent plane angle η_e is used to determine the direction of the equivalent plan and connect the shear plane and the equivalent plane, expressed as

$$\eta_e = \tan^{-1}\left(\frac{\tan\eta_c\cos\eta_{sh} + \sin(\varphi_n-\alpha_n)\sin\eta_{sh}}{\cos(\varphi_n-\alpha_n)}\right) \tag{15}$$

The shear flow angle η_{sh}, which characterizes the shear direction in primary shear zone, is given by Moufki and Dudzinski et al. [19].

$$\eta_{sh} = \tan^{-1}\left(\frac{\tan\lambda_s\cos(\varphi_n-\alpha_n)-\tan\eta_c\sin\varphi_n}{\cos\alpha_n}\right) \tag{16}$$

It is assumed that the orientation of chip velocity is collinear with the friction direction. The chip flow angle η_c can be calculated from the following implicit equation by the balance analysis of chip [19]:

$$\begin{cases}\tan\lambda_s\tan\beta_n\cos(\varphi_n-\alpha_n)\sin(\varphi_n-\alpha_n)\cos^2\eta_c-\tan\lambda_s\cos^2(\varphi_n-\alpha_n)\\ +\tan\eta_c\sin\varphi_n\cos(\varphi_n-\alpha_n)+(\cos\alpha_n-\sin\varphi_n\sin(\varphi_n-\alpha_n))\sin\eta_c\tan\beta_n=0\end{cases} \tag{17}$$

The shear zone is modeled as a parallel and equidistant formation in Oxley's model. However, many researchers proved that this zone is composed of wide region and narrow region. For instance, the main shear plane is not located in the middle of the shear band by a quick-stop micrograph from cutting steel [20]. The main shear plane AB is divided by the primary shear zone into two unequal parts, which are characterized by the portion $k(0<k<1)$, as shown in Fig. 3b. To describe the distribution of shear strain rate on non-equidistant shear model more realistically, Li et al. [21] assumed a piecewise power law distribution (for the detailed derivation of some important parameters and the governing equations for the shear strain rate $\dot{\gamma}$, the shear strain γ, and the temperature T, readers can refer to the literature [21]).

$$\dot{\gamma} = \begin{cases}\dfrac{\dot{\gamma}_m}{(kw)^q}y^q & z_e\in[0,kw]\\ \dfrac{\dot{\gamma}_m}{(1-k)^q w^q}(w-y)^q & z_e\in[kw,w]\end{cases} \tag{18}$$

$$\gamma = \begin{cases}\dfrac{\dot{\gamma}_m\cos\eta_e}{(q+1)V\cos\lambda_s\sin\varphi_n(kw)^q}{z_e}^{q+1} & z_e\in[0,kw]\\ -\dfrac{\dot{\gamma}_m\cos\eta_e}{(q+1)V\cos\lambda_s\sin\varphi_n(1-k)^q w^q}(w-z_e)^{q+1}+\dfrac{\cos\alpha_n\cos\eta_e}{\sin\varphi_n\cos\eta_s\cos(\varphi_n-\alpha_n)} & z_e\in[kw,w]\end{cases} \tag{19}$$

$$\frac{\partial T}{\partial z_e} = \frac{\cos\eta_e}{\rho_m C_p V\cos\lambda_s\sin\varphi_n}\chi\tau\dot{\gamma} \tag{20}$$

The main shear plane is defined as the plane in which the tangential velocity is equal to zero. The maximum shear strain rate $\dot{\gamma}_m$ and the unequal coefficient k are calculated according to the boundary condition of the tangential velocity of shear plane.

$$\dot{\gamma}_m = \frac{(q+1)V_s}{w} = \frac{(q+1)V\cos\lambda_s\cos\alpha_n}{w\cos\eta_{sh}\cos(\varphi_n-\alpha_n)} \tag{21}$$

$$k = \frac{\cos\eta_{sh}\cos(\varphi_n-\alpha_n)(\cos\varphi_n\cos\eta_{sh}+\tan\lambda_s\sin\eta_{sh})}{\cos\alpha_n} \tag{22}$$

$$V_c = \frac{V\cos\lambda_s\sin\varphi_n}{\cos\eta_c\cos(\varphi_n-\alpha_n)},\ V_s = \frac{V\cos\lambda_s\cos\alpha_n}{\cos\eta_s\cos(\varphi_n-\alpha_n)} \tag{23}$$

where V is the cutting velocity, V_c the chip velocity, and V_s the shear velocity.

Tool-chip interface friction is a critical factor in determining the quality of machining operations. Rake face will experience a high normal pressure, which yields sticking and sliding friction conditions when the material leaves the shear

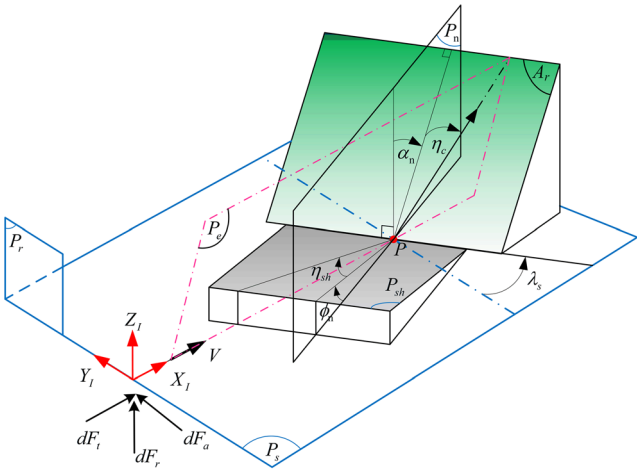

(a) Oblique cutting model and chip formation

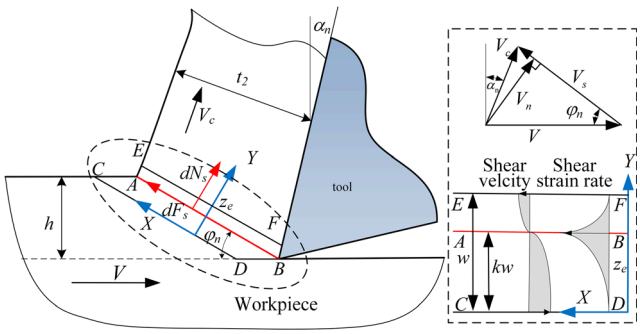

(b) Non-equidistant shear model

Fig. 3 Oblique cutting model and non-equidistant shear model [14]

zone. Different from the dual-zone model of the tool-chip interface based on the analytical thermomechanical model [22], the normal friction angle β_n is obtained from the following relationship:

$$\begin{cases} \mu_f = \tan\beta_n = \dfrac{\tau_1}{p_0}\left[1+\xi\left(1-\left(\dfrac{\tau_1}{p_0\mu_s}\right)^{1/\xi}\right)\right] \\ \dfrac{\tau_1}{p_0} = \dfrac{\xi+2}{4(\xi+1)}\dfrac{\sin[2(\varphi_n+\beta_n-\alpha_n)]}{\cos^2\beta_n} \end{cases} \tag{24}$$

where τ_1 is the shear yield strength of the workpiece material along the sticking region. p_0 is the normal pressure at the tool tip. ξ is the distribution exponent constant whose value is taken as 3, and μ_s is the sliding friction coefficient for tool-workpiece combination, which is considered as 0.8. μ_f is the apparent friction coefficient which is defined by the ratio between the total friction and normal forces acting on the rake face [22, 23]. By rearranging Eq. (27), one equation containing single unknown variable normal fraction angle β_n can be solved by the Newton-Raphson algorithm.

The normal shear angle φ_n is essential for estimating the apparent friction coefficient. It is assumed that the orthogonal shear angle is equal to the normal shear angle in oblique cutting. A modified Merchant equation is given as

$$\varphi_n = C_1 - C_2(\beta_n - \alpha_n) \tag{25}$$

where C_1 and C_2 are the empirical machining constants depending on the tool-workpiece material, which are taken as 0.69 and 0.5, respectively.

3.2 Estimation of the shear stress

The value of shear flow stress τ_{JC} has a significant effect on cutting forces. The Johnson-Cook model representing the material behavior has the advantage of simplicity and applicability, which is given as

$$\tau_{JC} = \frac{1}{\sqrt{3}}\left(A + B\left(\frac{\gamma}{\sqrt{3}}\right)^n\right)\cdot\left(1 + C\ln\left(\frac{\dot{\gamma}}{\dot{\gamma}_0}\right)\right)\cdot\left(1-\left(\frac{T-T_r}{T_m-T_r}\right)^m\right) \tag{26}$$

where γ, $\dot{\gamma}$, and T represent the shear strain, the shear strain rate, and the working temperature, respectively. $\dot{\gamma}_0 = 1s^{-1}$ devotes the reference shear strain rate, T_r is the room temperature, and T_m is the melting temperature of the workpiece. A is the yield strength of the material, B is the strength coefficient, and C is the strain rate sensitivity coefficient. Strain hardening exponent and thermal softening coefficient are characterized by exponent constant n and m, respectively.

Material size effect caused by the variable IUCT in the primary shear zone is an important characteristic in the machining progress. It is worth noting that the IUCT varies distinctly for variable helix end mill, especially due to the existence of the cutter runout. To account for the size effect, a modified Johnson-Cook model developed by Joshi and Suhas et al. [24] is used, which is derived by including the strain gradient plasticity based on the Taylor's dislocation principle.

$$\tau_s = \tau_{JC}\sqrt{1+\left(\frac{\alpha_c^2 G^2 b_g \eta}{\tau_{JC}^2}\right)^u} \tag{27}$$

where α_c is the empirical constant, G is the shear modulus of workpiece, b_g is the magnitude of the Burgess vector, and u is the exponential factor. The strain gradient η is determined by

$$\begin{cases} \eta = \dfrac{1}{L} \\ L = \dfrac{h}{\sin\varphi_n} \end{cases} \tag{28}$$

where L is the length of the primary shear zone and h is the IUCT. By substituting Eq. (28) into Eq. (27), it can be seen that the modified shear stress is inversely proportional to the IUCT for a constant shear angle.

Table 1 Properties of workpiece material Al6061-T6

Johnson-Cook parameter							
A (MPa)	B (MPa)	C	n	m	$\dot{\gamma}_0$ (1/s)	T_m (°C)	T_r (°C)
324	114	0.02	0.42	1.34	1	582	25
Material properties							
ρ_m (kg/m^3)	C_p (J/kg K)	k_p (W/mK)	χ	G (GPa)	α_c	b_g (nm)	u
2700	896	167	0.85	26	0.5	0.286	1

Source: [25]

4 Estimation of cutting force coefficients

4.1 Shearing force coefficients in primary shear zone

In the primary deform zone, the shearing force in the shearing plane is decomposed into two force components. The shear force dF_s is proportional to the shear stress τ_s in the primarily shear zone. The normal force dN_s is perpendicular to the shear plane, in Fig. 3b.

$$\begin{cases} dF_s = \tau_s \dfrac{dz{\cdot}h}{\cos\lambda_s \sin\varphi_n} \\ dN_s = dF_s \dfrac{\cos\eta_{sh}[\sin(\varphi_n - \alpha_n) + \tan\beta_n \cos\eta_c \cos(\varphi_n - \alpha_n)]}{\cos(\varphi_n - \alpha_n) - \tan\beta_n \cos\eta_c \sin(\varphi_n - \alpha_n)} \end{cases} \tag{29}$$

According to the geometrical transformation relations in Fig. 3, the tangential, radial, and axial cutting force components applied to the oblique element P can be calculated from the following matrix form:

$$\begin{bmatrix} dF_{i,j,t} \\ dF_{i,j,r} \\ dF_{i,j,a} \end{bmatrix} = \begin{bmatrix} \cos\lambda_s \cos\varphi_n \cos\eta_{sh} + \sin\lambda_s \sin\eta_{sh} & \cos\lambda_s \sin\varphi_n \\ -\sin\varphi_n \cos\eta_{sh} & \cos\varphi_n \\ \sin\lambda_s \cos\varphi_n \cos\eta_{sh} - \cos\lambda_s \sin\eta_{sh} & \sin\lambda_s \sin\varphi_n \end{bmatrix} \cdot \begin{bmatrix} dF_s \\ dN_s \end{bmatrix} \tag{30}$$

Substituting Eq. (29) into Eq. (30), the three cutting force components can be rewritten as

$$\begin{cases} dF_{i,j,t} = \dfrac{dz{\cdot}h{\cdot}\tau_s}{\cos\lambda_s \sin\varphi_n} \cdot \dfrac{\cos\eta_{sh}[\cos\alpha_n \cos\lambda_s + \tan\beta_n(\sin\eta_c \sin\lambda_s + \cos\eta_c \sin\alpha_n \cos\lambda_s)]}{\cos(\varphi_n - \alpha_n) - \tan\beta_n \cos\eta_c \sin(\varphi_n - \alpha_n)} = K_{tc} dz{\cdot}h \\ dF_{i,j,r} = \dfrac{dz{\cdot}h{\cdot}\tau_s}{\cos\lambda_s \sin\varphi_n} \cdot \dfrac{\cos\eta_{sh}(-\sin\alpha_n + \tan\beta_n \cos\eta_c \cos\alpha_n)}{\cos(\varphi_n - \alpha_n) - \tan\beta_n \cos\eta_c \sin(\varphi_n - \alpha_n)} = K_{rc} dz{\cdot}h \\ dF_{i,j,a} = \dfrac{dz{\cdot}h{\cdot}\tau_s}{\cos\lambda_s \sin\varphi_n} \cdot \dfrac{\cos\eta_{sh}[\cos\alpha_n \sin\lambda_s + \tan\beta_n(-\sin\eta_c \sin\lambda_s + \cos\eta_c \sin\alpha_n \sin\lambda_s)]}{\cos(\varphi_n - \alpha_n) - \tan\beta_n \cos\eta_c \sin(\varphi_n - \alpha_n)} = K_{ac} dz{\cdot}h \end{cases} \tag{31}$$

By dividing the cutting forces $dF_{i,j,t}$, $dF_{i,j,r}$, and $dF_{i,j,a}$ by the chip load $dz \cdot h$, the shearing force coefficients K_{tc}, K_{rc}, and K_{ac} are estimated through the expressions given in the following [13]:

$$\begin{cases} K_{tc} = \dfrac{\tau_s{\cdot}\cos\eta_{sh}[\cos\alpha_n \cos\lambda_s + \tan\beta_n(\sin\eta_c \sin\lambda_s + \cos\eta_c \sin\alpha_n \cos\lambda_s)]}{\cos\lambda_s \sin\varphi_n[\cos(\varphi_n - \alpha_n) - \tan\beta_n \cos\eta_c \sin(\varphi_n - \alpha_n)]} \\ K_{rc} = \dfrac{\tau_s{\cdot}\cos\eta_{sh}(-\sin\alpha_n + \tan\beta_n \cos\eta_c \cos\alpha_n)}{\cos\lambda_s \sin\varphi_n[\cos(\varphi_n - \alpha_n) - \tan\beta_n \cos\eta_c \sin(\varphi_n - \alpha_n)]} \\ K_{ac} = \dfrac{\tau_s{\cdot}\cos\eta_{sh}[\cos\alpha_n \sin\lambda_s + \tan\beta_n(-\sin\eta_c \sin\lambda_s + \cos\eta_c \sin\alpha_n \sin\lambda_s)]}{\cos\lambda_s \sin\varphi_n[\cos(\varphi_n - \alpha_n) - \tan\beta_n \cos\eta_c \sin(\varphi_n - \alpha_n)]} \end{cases} \tag{32}$$

4.2 Edge force coefficients in tertiary zone

Owing to the limitations of tool manufacturing technology, it is inevitable that the cutting edges have certain radius rather than perfectly sharp. As the chip thickness reduces to dimensions comparable with that of the tool edge radius, the edge effect is more dominant than cutting shear effect. Therefore, the edge radius needs to be considered in the calculation of edge forces.

The normal rake angle at the cutting edge radius is more negative when the depth of cut is less than the edge radius of the cutter r_e. Depending on the relation between IUCT and edge radius, the normal rake angle α_n is replaced by the partial effective rake angle α_{ref} [26].

$$\alpha_{ref} = \begin{cases} \alpha_n & (h > h_{\lim}) \\ \sin^{-1}(h/r_e - 1) & (h \le h_{\lim}) \end{cases} \tag{33}$$

where $h_{\lim}$ is the limiting value of IUCT and it is defined by

$$h_{\lim} = r_e \cdot (1 + \sin\alpha_n) \tag{34}$$

The edge force coefficients K_{te}, K_{re}, and K_{ae} can be estimated from the analytical model proposed by Abdelmoneim and Scrutton [27]. The slip-line field model developed by Waldorf et al. [28] is one of the most popular models. In the slip-line field model, the radial edge force coefficient K_{ae} is usually taken as zero and the alternative value of K_{ae} can also be estimated by the approach proposed by Armarego and Deshpande [29]. The equations are given as

$$\begin{cases} K_{te} = \dfrac{\tau_s\left[\left(1 + 2\alpha_0 + 2\gamma_0 + \sin(2\eta_0)\sin\left(\varphi_n - \alpha_{ref} + \eta_0\right) + \cos(2\eta_0)\cos\left(\varphi_n - \alpha_{ref} + \eta_0\right)\right)\right]R}{\sin\eta_0} \\ K_{re} = \dfrac{\tau_s\left[\left(1 + 2\alpha_0 + 2\gamma_0 + \sin(2\eta_0)\cos\left(\varphi_n - \alpha_{ref} + \eta_0\right) - \cos(2\eta_0)\sin\left(\varphi_n - \alpha_{ref} + \eta_0\right)\right)\right]R}{\sin\eta_0} \\ K_{ae} = K_{te}\sin(i) \ \text{ or } \ 0 \end{cases} \tag{35}$$

5 Simulation and experimental validation

A series of milling tests without coolant are conducted in the CNC machining center. The workpiece material selected for the experiments is Al6061-T6. The three-fluted flat end mills made of cemented carbide are used, which have the same 8-mm diameter, 5° normal rake angle, and 0.02-mm edge radius. Four different types of end mills are shown in Fig. 6; each has different helix angles and pitch angles. The cutting parameters in the test are shown in Table 2. The corresponding computer programs in Matlab R2014a are developed to implement on the analysis of the cutting force model. The flowchart of the cutting force calculation is shown in Fig. 4. The properties of workpiece material Al6061-T6 are listed in Table 1.

The experimental setup is shown in Fig. 5. The workpiece is fixed on a Kistler 9257b dynamometer. The lower part of the dynamometer is fixed on the workbench. The experimental cutting force components in the three X, Y, and Z directions are measured using a Kistler 9257b dynamometer. The sampling frequency of

Table 2 Cutting parameters for milling tests

Test No.	Milling type	Rotation speed n (r/min)	Axial depth of cut a_p (mm)	Radial depth of cut a_r (mm)	Feed per tooth f_z (mm/z)
1	Down	1000	2	2	0.10
2	Up	1000	2	2	0.10
3	Down	1000	1.8	3	0.10
4	Up	1000	1.8	3	0.10
5	Down	1000	1.5	4	0.10
6	Up	1000	1.5	4	0.10
7	Down	1000	1.2	5	0.10
8	Up	1000	1.2	5	0.10
9	Down	1000	1	6	0.10
10	Up	1000	1	6	0.10
11	Down	1000	0.5	7	0.10
12	Up	1000	0.5	7	0.10

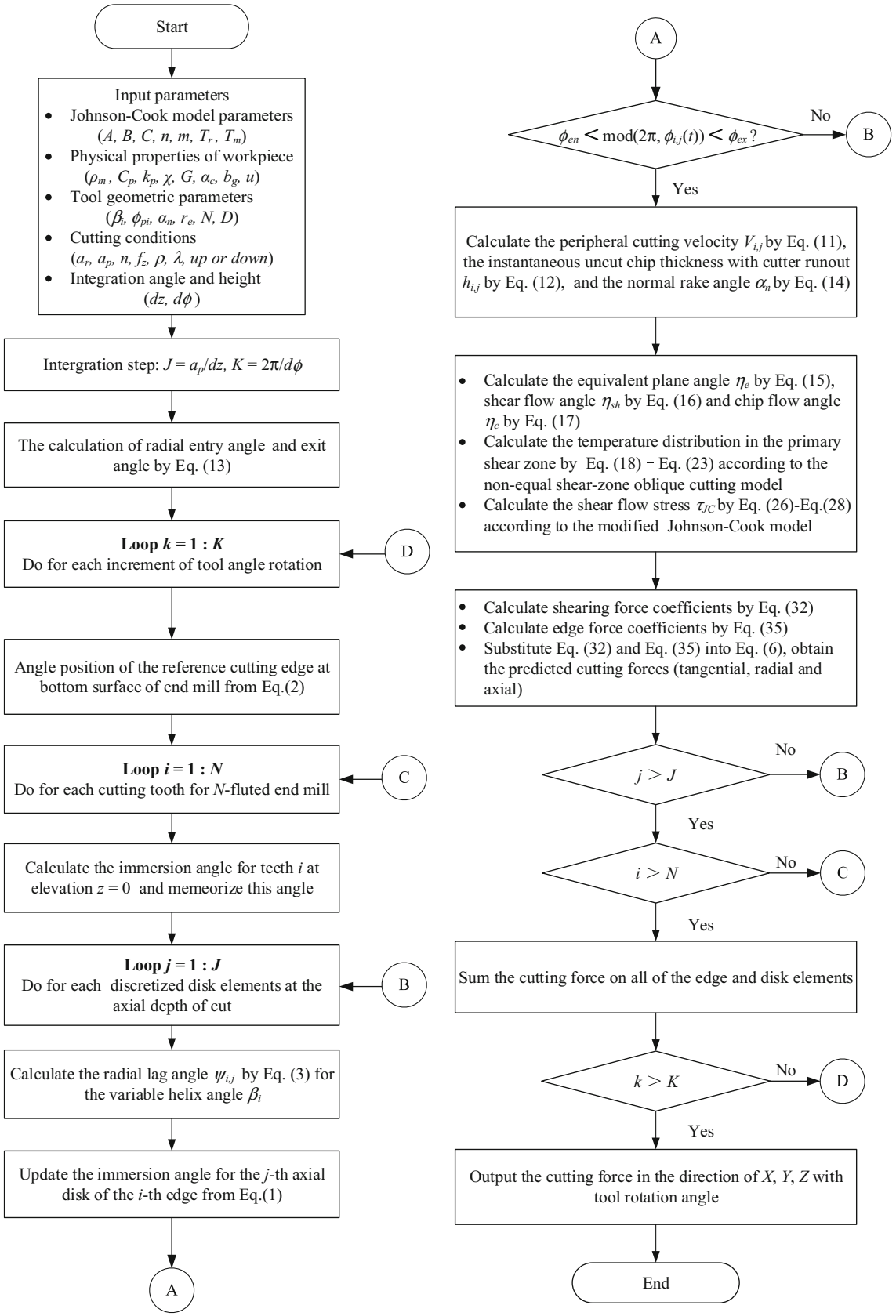

Fig. 4 The flowchart of the cutting force calculation

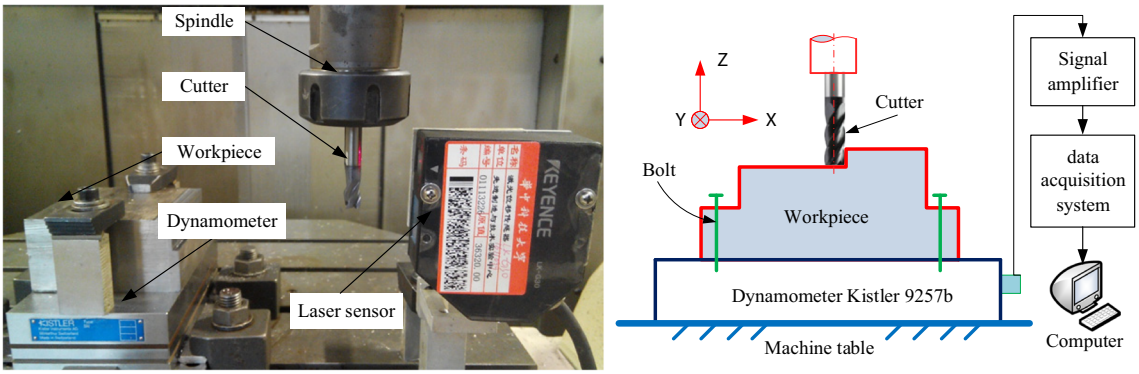

Fig. 5 Force measurement system

the dynamometer is 20 KHz. The predicted cutting force components are calculated according to the flowchart as shown in Fig. 4.

5.1 Cutter runout

Cutter runout is a common phenomenon due to the tool dimensional errors, insert settings, and thermal deformation. The presence of cutter runout will redistribute the IUCT and the cutting forces in multi-fluted milling process. It can be seen from Figs. 7, 8, 9, and 10 that the cutter runout exists in those milling tests. In order to calculate the cutting forces more precisely, the radial cutter runout is considered in the analytical force model. The unknown runout parameters are obtained by laser sensor measurement. The detailed method can refer to the literature [30]. The cutter runout parameters for four different types of end mills are given in Table 3.

5.2 Comparison with regular end mill

In order to illustrate the effectiveness of the proposed analytical model, the predicted instantaneous cutting forces for one revolution are used to compare with the measured cutting forces. The measured cutting forces are taken as the average values of the cutting forces measured in the neighboring ten periods. The comparisons for uniform end mill A are shown in Fig. 7. It is seen that the predicted cutting forces in X, Y, and Z directions are essentially consistent with the measured cutting forces, in despite of different cutting conditions and milling type. Although the peak cutting forces of one tooth for uniform end mill have slightly different due to the presence of cutter runout, the waveform of the cutting forces has the same trend.

Table 3 Cutter runout parameters in the proposed analytical model

Cutter type	Runout amplitude ρ (μm)	Runout angle λ (deg)
End mill A	5.6	45.1
End mill B	3.5	30.8
End mill C	4.3	20.6
End mill D	2.3	32.3

5.3 Comparison with variable helix end mill

The variable helix angle end mill B and variable pitch angle end mill C in Fig. 6 are used to investigate the effects of helix angle and pitch angle on the cutting forces, respectively. The comparisons between the predicted cutting forces and measured cutting forces are listed in Figs. 8 and 9, respectively. The results show that the experimental values of cutting forces are in good agreement with the predicted cutting forces. Besides, some experiments are conducted with the end mill D, which is the combination of various pitch angle and helix angle. As shown in Fig. 10, the experimental results agree well with the simulated results.

As quantitative analysis is very efficient to characterize the accuracy of theoretical model, two levels of quantitative analysis comparisons are carried out. The detailed method and some defined terms are referred in [31]. In the first level of comparison, the amplitudes of the cutting force of each tooth are calculated. Then, the varying amplitudes of each tooth are averaged to a single value for reducing the effect of cutter runout and obtaining a better comparison. The average amplitudes of the cutting forces from experiment measurement $Exp_{(amp)}$ and predicted model $Pre_{(amp)}$ are listed in Table 4. The computed results of error percentage $Error$ (%) for feed force Fx, transverse force Fy, and axial force Fz are also given in Table 4. In the present work, the average of absolute errors is taken as a measure of performance of the proposed model. It is seen that most of the average error is within 15% for four types of cutter in all direction.

In the second level of comparison, the force variations with cutter rotation are analyzed to include both

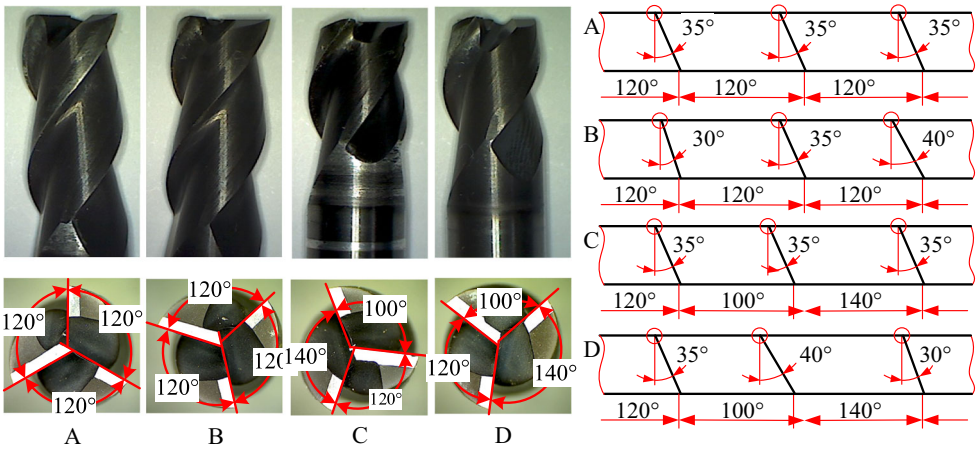

Fig. 6 Uniform end mill and variable pitch and variable helix end mills. **a** End mill *A* with 35°/35°/35° helix angle and 120°/120°/120° pitch angle. **b** End mill *B* with 30°/35°/40° helix angle and 120°/120°/120° pitch angle. **c** End mill *C* with 35°/35°/35° helix angle and 120°/100°/140° pitch angle. **d** End mill *D* with 35°/40°/30° helix angle and 120°/100°/140° pitch angle

(a) End mill A with 35° /35° /35° helix angle and 120° /120° /120° pitch angle,
(b) End mill B with 30° /35° /40° helix angle and 120° /120° /120° pitch angle,
(c) End mill C with 35° /35° /35° helix angle and 120° /100° /140° pitch angle,
(d) End mill D with 35° /40° /30° helix angle and 120° /100° /140° pitch angle.

Table 4 Comparison analysis of experimental cutting forces and predicted cutting forces

Cutter type	No.	Feed force *Fx*				Transverse force *Fy*				Axial force *Fz*			
		$Exp_{(amp)}$ (N)	$Pre_{(amp)}$ (N)	*Error* (%)	*Abs. dev* (%)	$Exp_{(amp)}$ (N)	$Pre_{(amp)}$ (N)	*Error* (%)	*Abs. dev* (%)	$Exp_{(amp)}$ (N)	$Pre_{(amp)}$ (N)	*Error* (%)	*Abs. dev* (%)
Cutter A	1	102.19	102.64	−0.44	4.57	240.95	245.54	−1.87	1.27	40.21	43.25	−7.03	−4.95
	2	244.80	232.28	5.39	4.86	104.81	133.46	−21.47	−1.70	42.70	43.46	−1.75	−2.87
	7	161.65	155.66	3.85	3.50	180.26	158.71	13.58	−3.66	32.19	29.80	8.02	−9.89
	8	145.61	128.84	13.02	−3.67	195.79	178.58	9.64	0.86	32.91	29.80	10.44	−13.76
	11	82.96	84.74	−2.10	−4.43	36.63	42.50	−13.81	4.37	10.69	9.26	15.44	−78.17
	12	68.52	60.20	13.82	1.54	83.57	77.84	7.36	0.75	15.69	8.94	75.50	−100.65
	Average error (abs)			6.44	3.76	Average error (abs)		12.07	2.37	Average error (abs)		8.54	21.93
Cutter B	1	104.28	98.54	5.83	2.85	251.25	234.10	7.33	0.97	41.64	43.73	−4.78	−6.16
	3	122.30	113.94	7.34	3.71	257.98	241.00	7.05	0.71	41.90	45.68	−8.27	−4.37
	7	162.57	150.45	8.06	2.59	171.15	149.53	14.46	−4.34	30.84	30.06	2.59	−12.85
	8	153.33	123.70	23.95	−4.54	177.00	169.65	4.33	3.95	34.16	30.06	13.64	−14.10
	9	155.04	152.89	1.41	2.02	130.27	108.65	19.90	0.26	26.90	17.75	51.55	−4.46
	10	119.59	109.89	8.83	−3.39	164.77	154.60	6.58	1.41	22.56	18.16	24.23	−15.06
	Average error (abs)			9.32	3.14	Average error (abs)		10.86	2.10	Average error (abs)		14.90	10.64
Cutter C	1	102.95	99.76	3.20	3.95	233.23	232.09	0.49	0.22	42.17	40.31	4.61	−1.76
	3	114.79	109.18	5.14	4.04	257.07	239.08	7.52	−0.99	45.67	41.84	9.15	−3.30
	5	136.03	144.07	−5.58	2.53	217.09	202.56	7.17	−0.41	41.88	37.17	12.67	−5.22
	6	191.31	165.67	15.48	−0.38	206.96	202.36	2.27	1.11	45.08	37.31	20.83	−8.23
	11	81.53	77.77	4.83	−4.50	53.23	55.64	−4.33	5.26	12.17	12.69	−4.10	−57.09
	12	74.52	64.50	15.53	0.96	82.44	73.34	12.41	5.38	12.36	11.05	11.86	−69.93
	Average error (abs)			7.26	3.09	Average error (abs)		5.44	1.68	Average error (abs)		11.04	14.37
Cutter D	3	116.90	107.29	8.96	4.17	254.06	238.65	6.46	0.13	43.46	41.90	3.72	−1.95
	5	148.88	141.94	4.89	3.04	221.21	203.20	8.86	0.27	40.69	37.41	8.77	−5.98
	6	193.07	166.67	15.84	0.22	202.94	201.30	0.81	1.59	46.40	37.60	23.40	−5.47
	8	158.18	122.55	29.07	−4.59	184.17	166.82	10.40	4.20	30.44	28.25	7.75	−1.36
	11	80.25	78.15	2.69	−6.81	54.84	57.49	−4.61	6.52	14.55	14.00	3.93	−33.1
	12	70.48	66.29		4.99	80.33	75.09	6.98	3.57	14.62	12.68	15.30	−57.83
	Average error (abs)			11.45	3.65	Average error (abs)		6.10	2.40	Average error (abs)		9.77	10.37

amplitude variation and dc component in the comparison. The absolute deviation *Abs.dev* (%) between experimental forces and predicted forces is also listed in Table 4. The most of average absolute deviation for four types of cutter in the all direction are within 10%. Those results of quantitative analysis verify the effectiveness and consistency of the proposed model. It is also seen that the value of most absolute deviations for *Fx* and *Fy* are less than axial force *Fz*. This is resulted from the fact that the additional axial cutting force caused by end-cutting edge is not considered in the proposed model, and the real experimental process exists in the end-cutting edge and back-cutting phenomenon.

The qualitative analysis in Figs. 7, 8, 9, and 10 and quantitative analysis in Table 4 all show that the predicted cutting forces from the analytical model are in good agreement with the measured cutting forces for four types of cutter in all cutting direction. However, there are still small amounts of deviations in some local areas. The main reasons for this deviation may be contributed to the following factors: (1) the accurate calculations of shear angle, friction angle, shear flow angle, and flow stress, etc. parameters in the proposed analytical model; (2) the inhomogeneous distribution of workpiece's properties, such as the hardness and the chemical composition; (3) the flank wear of cutter in machining process and the stiffness of cutter under different axial depth of cut; (4) the precision of data collected by a dynamometer, such as the effects of the inevitable noise and the bandwidth of dynamometer; and (5) although the classical static radial cutter out is considered in the model, the cutter runout is dynamic due to cutting force

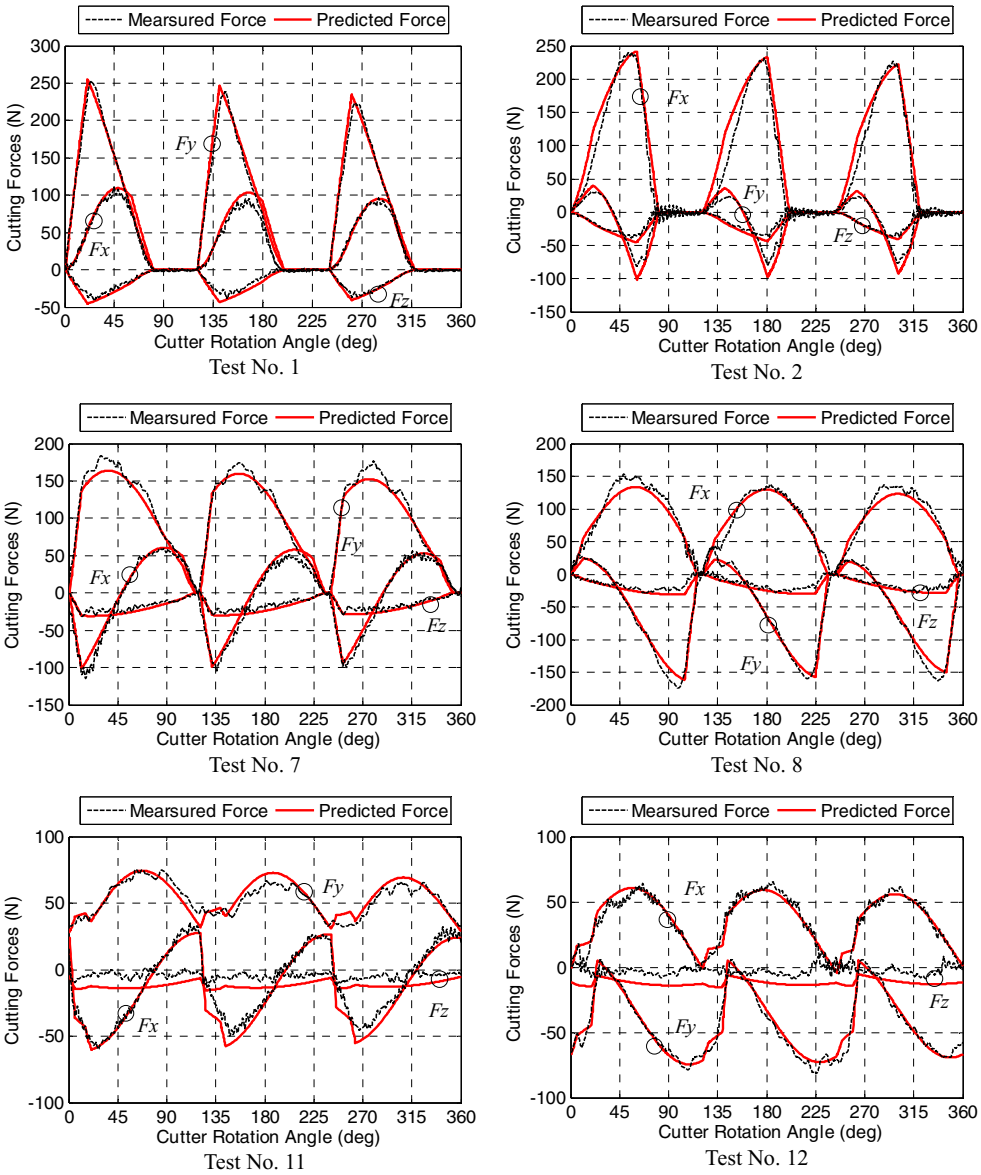

Fig. 7 Comparison of measured and predicted cutting forces for end mill A

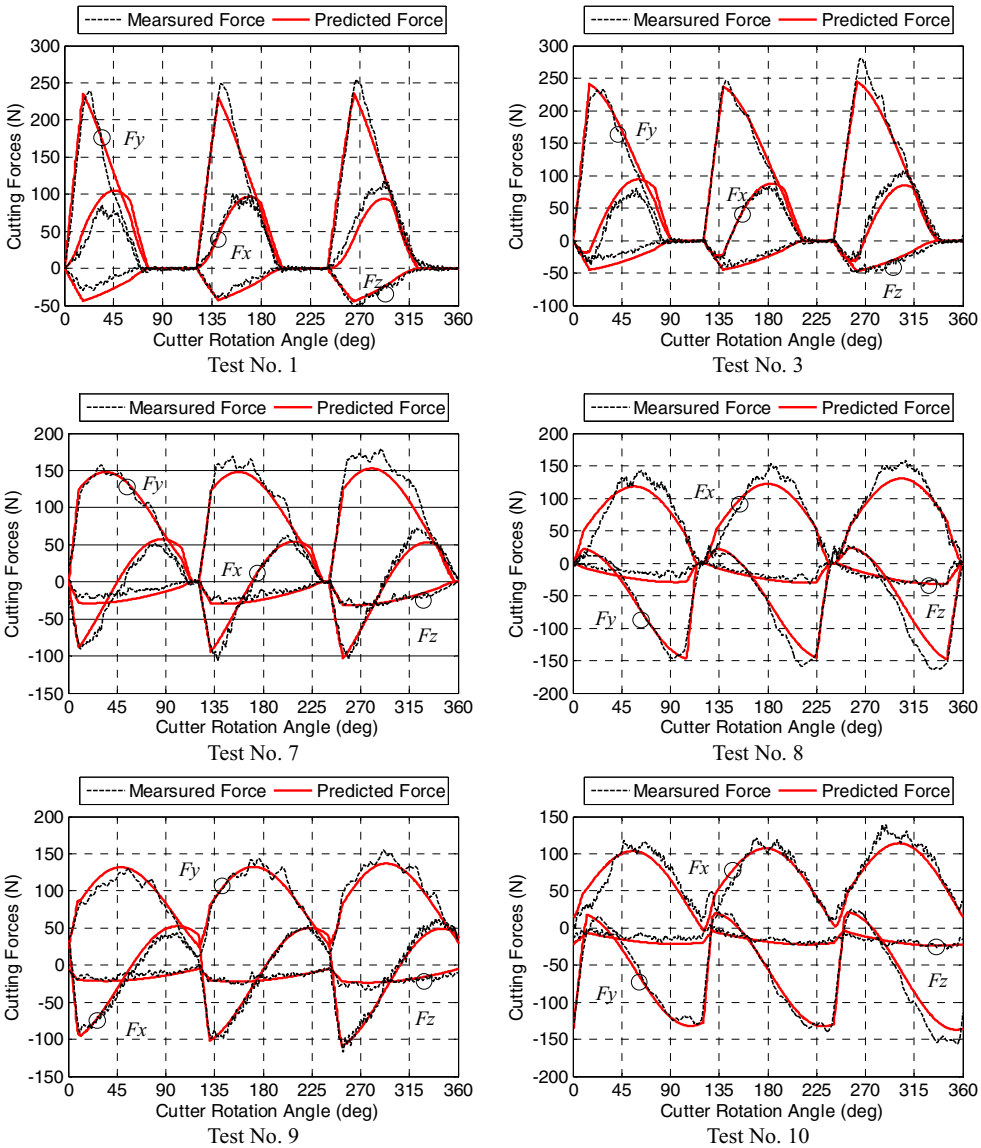

Fig. 8 Comparison of measured and predicted cutting forces for end mill B

variation, spindle and tool imbalance, and non-uniform progression of tool wear [32].

6 Effect of tool geometries and milling parameters on cutting forces

Tool geometries and milling parameters are incorporated in the unified analytical cutting force model. It is meaningful to analyze the influence of the different parameters on cutting forces. The default conditions for all simulated cases are down-milling, three-fluted, diameter 8 mm, spindle speed 1000 r/min, radial depth of cut 4 mm, depth of cut 2 mm, feed per tooth 0.1 mm/fz, rake angle 5°, helix angle 35°/40°/30°, and pitch angle 120°/100°/140°. The simulated cases in the following only change the research variable while the other parameters maintain default.

6.1 Effect of tool geometries on cutting forces

6.1.1 Effect of helix angle β

The effect of helix angle on cutting forces in actual milling tests is compared in Fig. 7 (test Nos. 1, 7, 8) with Fig. 8 (test Nos. 1, 7, 8). The simulation show that the helix angle has an effect on the duration time of cutting forces for each tooth from cut-in stage to cutout stage, as shown in Fig. 11. As shown in Eq. (3), the radial lag angle increases with the increase of the helix angle. Then, the duration time will be longer in cut-out stage with the larger helix angle. Cutting forces for each tooth decrease with the increase of the helix angle. It can be explained by that the number of discrete oblique elements at certain axial depth of cut is the same without the effect of the helix angle. The increase of the

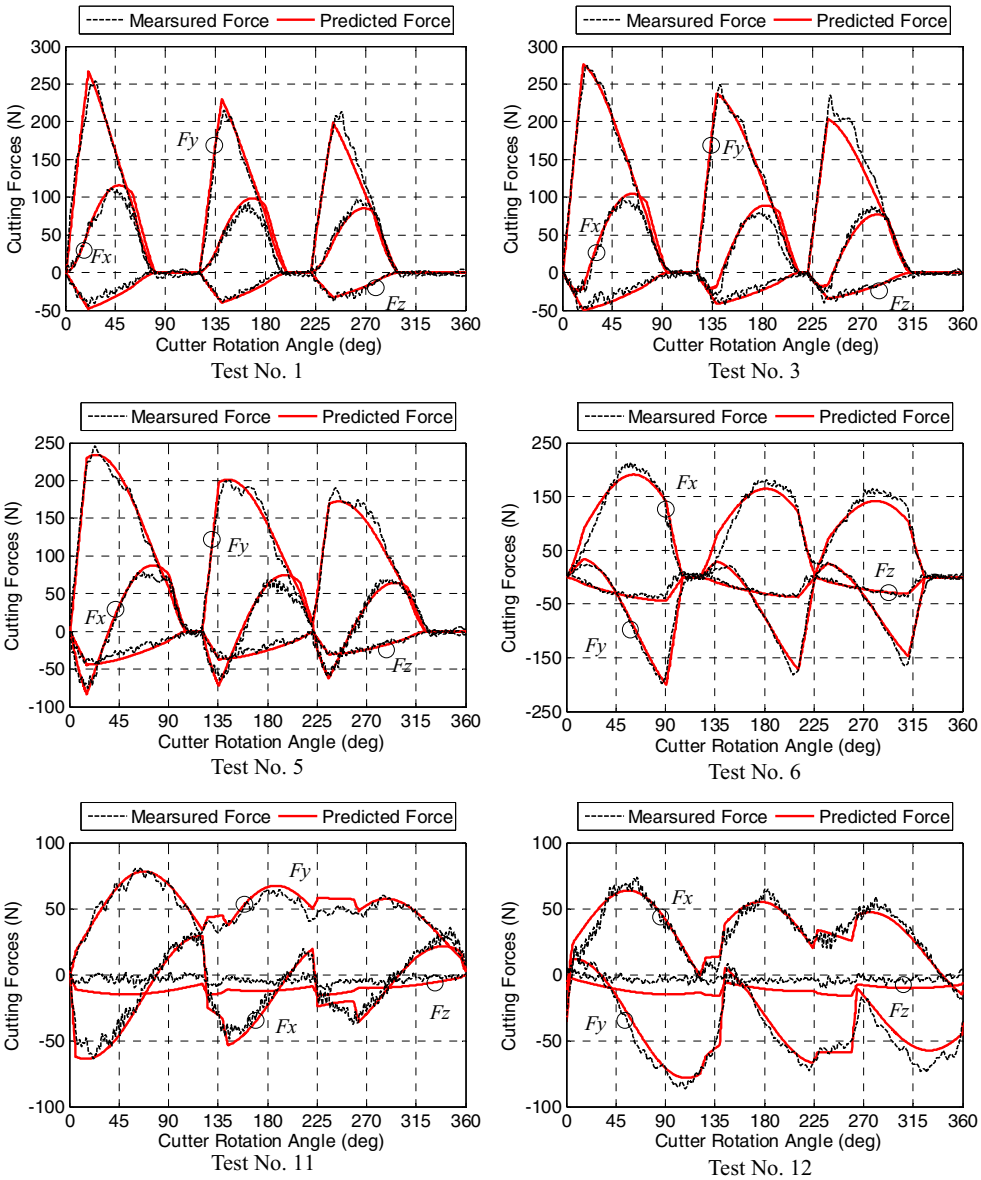

Fig. 9 Comparison of measured and predicted cutting forces for end mill C

helix angle will lead to less oblique elements involved in cutting when the tool rotates to same angular position.

6.1.2 Effect of pitch angle ϕ_p

One can compare Fig. 7 (test Nos. 1, 11, 12) with Fig. 9 (test Nos. 1, 11, 12) in terms of the effect of pitch angle on cutting forces in actual milling tests. Similarly, it can be seen from Fig. 12 that the pitch angles have a direct effect on the peak cutting force components. The peak cutting force of each tooth is the same for uniform end mill. However, the peak cutting force of each tooth is different for variable pitch end mill due to the variable cutting load between adjacent cutting teeth. The peak cutting forces increase with the increase of pitch angle. The excessive peak cutting force will be a great damage to the cutting edge. Therefore, the selection of pitch angle should consider the effects of cutting edge strength and cutting stability.

6.1.3 Effect of rake angle α_n

As shown in Fig. 13, the duration time of cutting forces from cut-in stage to peak cutting forces does not change. However, both cutting force components are observed to have a decreasing trend as the rake angle increased from negative to positive values. The effect of rake angle on the cutting force in the direction of *Fx* and *Fz* is more obvious than that on the cutting force in the direction of *Fy*. The decreasing trend can be

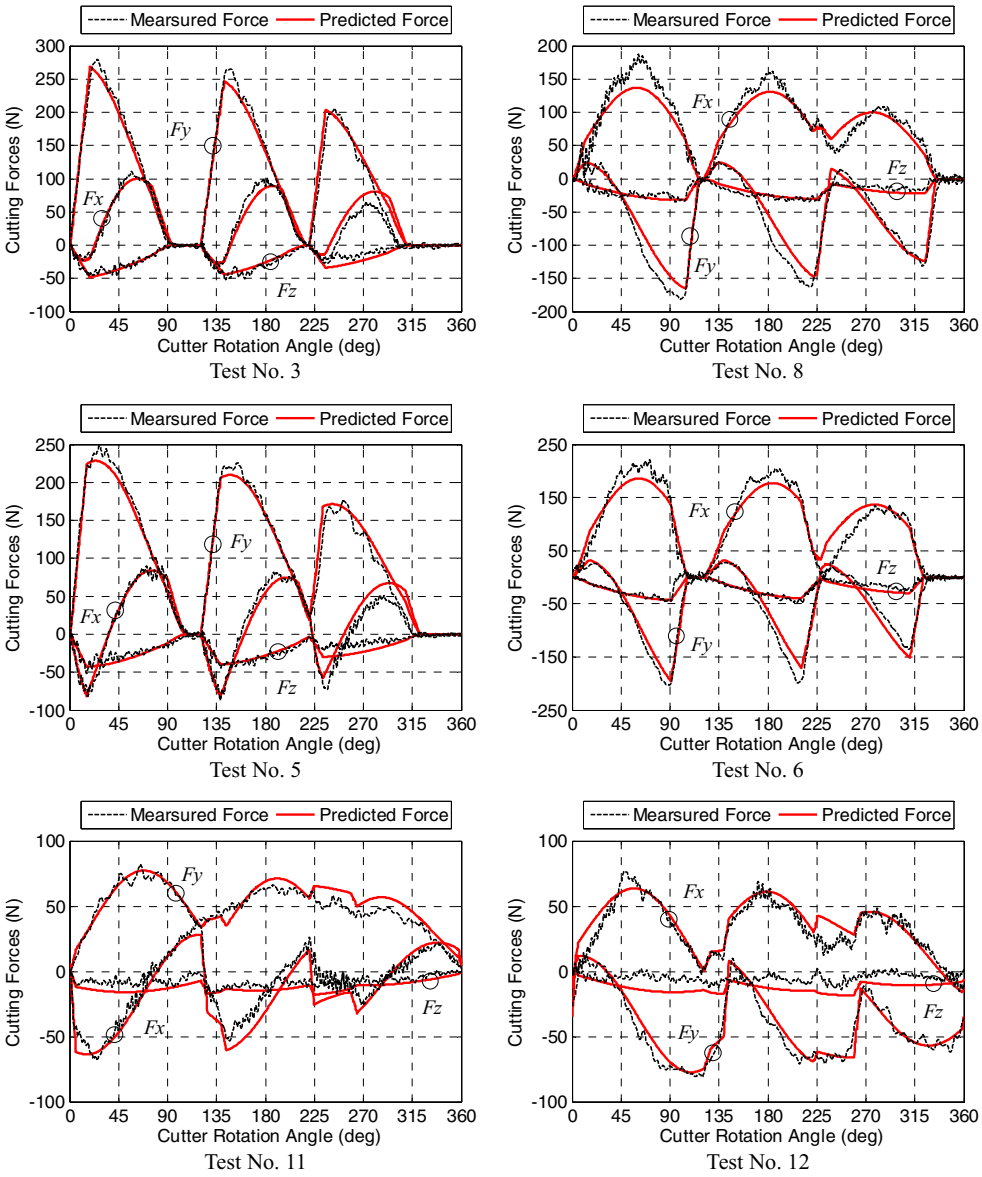

Fig. 10 Comparison of measured and predicted cutting forces for end mill D

explained by the increase of shear angle and the reduction of tool-chip contact length. By decreasing the rake angle in negative, the shear angle increases and the contact length decreases, which will lead to the decrease of cutting forces. By

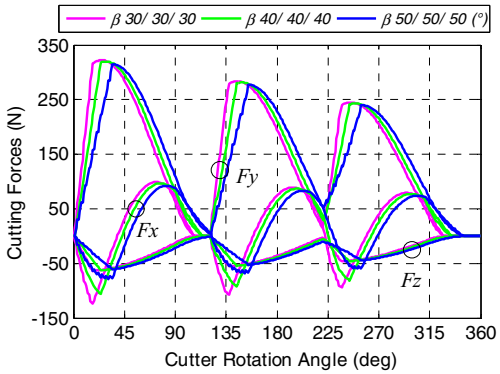

Fig. 11 Influence of the helix angle on the cutting forces

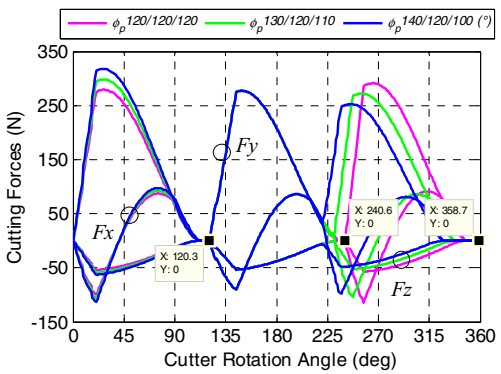

Fig. 12 Influence of the pitch angle on the cutting forces

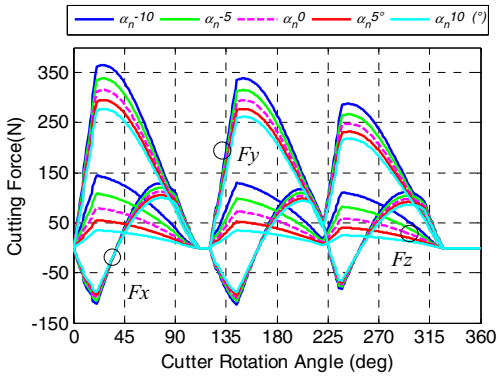

Fig. 13 Influence of the rake angle on the cutting forces

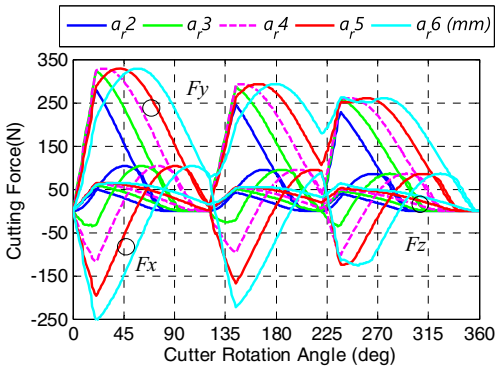

Fig. 15 Influence of the radial depth of cut on the cutting forces

increasing the rake angle in positive, the tool-chip contact length decreases and the shear angle decreases, which will result in the decrease of friction force.

6.2 Effect of milling parameters on cutting forces

6.2.1 Effect of axial depth of cut a_p

It is observed from Fig. 14 that both cutting force components increase with the increase of axial depth of cut. The increase of axial depth of cut causes the increase of contact zones between tool and workpiece, and more material is removed from the workpiece at the same time. Although the axial depth of cut has no effect on the slope of cutting forces in cut-in stage, the distribution of cutting forces in cut-out stage is changed due to the presence of cutter's helix angle. Therefore, the duration time of cutting forces from cut-in stage to peak cutting forces increases with the increase of axial depth of cut.

6.2.2 Effect of radial depth of cut a_r

As shown in Fig. 15, it is obvious that the duration time of cutting forces for each tooth increases with the increase of radial depth of cut through changing the radial entry angle and exit angle. The radial depth of cut also has an important effect on the distribution of cutting forces. By increasing the radial depth of cut from 2 to 4 mm, the peak cutting force of *Fy* is increasing by means of increasing the maximal uncut chip thickness. When the radial depth of cut is over the tool radius, the value of peak cutting force does not change. Moreover, the position of peak cutting force shifts toward to the right due to that more than one teeth are always cutting material in cutting process. However, the cutting force *Fx* will appear some negative cutting force when the radial depth of cut is increasing from 4 to 6 mm. The value and position of peak cutting force for *Fx* in positive is similar to *Fy*. The value of peak cutting force for *Fx* in negative increases with the increase of radial depth of cut.

6.2.3 Effect of feed rate per tooth f_z

As shown in Fig. 16, it is observed that all the cutting force components increase as the feed rate increases. The reason for this increase of cutting forces with the increase of the feed rate per tooth is due to an increase of chip load per tooth as the feed rate increases. The feed rate per tooth has no influence on the duration time of cutting forces for each tooth. The value of peak cutting forces increases with the increase of feed rate per tooth. It is should be noted that the value of peak cutting forces for each tooth differs greatly in the condition of small feed rate and large cutter runout.

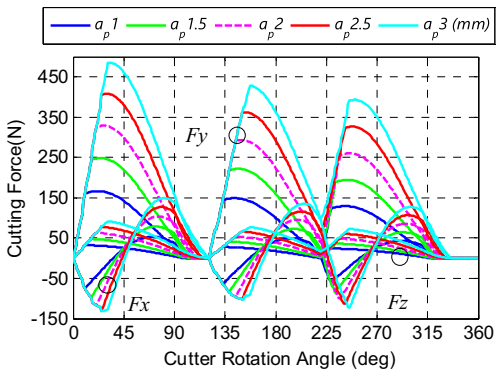

Fig. 14 Influence of the axial depth of cut on the cutting forces

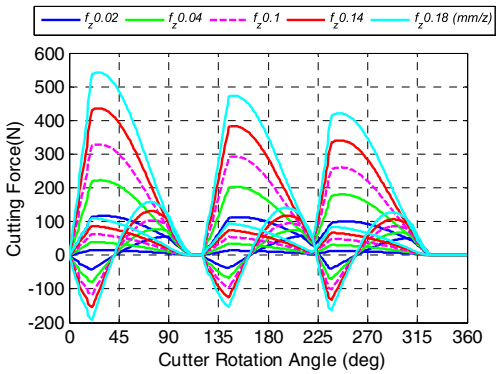

Fig. 16 Influence of the feed rate per tooth on the cutting forces

7 Conclusions

A unified analytical cutting force model for variable helix end mill is developed in this paper. A series of milling tests with four types of end mills are implemented in the CNC machining center for demonstrating the validity and consistency of the proposed model. With respect to the previous mechanistic model, the contributions of the proposed model are drawn as follows:

1. The unified analytical cutting force model associates variable tool geometries, milling parameters, and cutting forces during milling process. Several simulated cases are carried out for revealing the effects of tool geometries and milling parameters on cutting forces, which are benefit for the design and optimization of variable helix end mills.
2. A modified Johnson-Cook model accounting for the material size effect is introduced to estimate the shear flow stress in primary shear zone. In the tertiary zone, edge radius and the partial effective rake angle involved in the calculation of edge force are included in the analytical model in order to take into account the rubbing effect precisely.
3. The proposed analytical approach calculates the cutting force components only from the input parameters, the workpiece material properties, tool geometry, and cutting condition. Therefore, the analytical model is an alternative method which avoids laborious experimental calibration compared with the classical mechanistic approach.

It is worth noticing that the cutter experienced deflection and flank wear caused by the weak stiffness and high temperature during practical cutting process. Consequently, these effects need to be investigated in future work for more accurate prediction of cutting forces.

Acknowledgements The authors are grateful to the "973" National Basic Research Program of China (Grant No. 2015CB057304) and the National Natural Science Foundation of China (Grant No. 51305151, No. 51535004) for supporting the work.

References

1. Arrazola PJ, Özel T, Umbrello D, Davies M, Jawahir IS (2013) Recent advances in modelling of metal machining processes. Cirp Ann-Manuf Techn 62(2):695–718
2. Tlusty J, MacNeil P (1975) Dynamics of cutting forces in end milling. Ann CIRP 24(1):21–25
3. Kline WA, DeVor RE (1983) The effect of runout on cutting geometry and forces in end milling. Int J Mach Tools Manuf 23(2):123–140
4. Gradišek J, Kalveram M, Weinert K (2004) Mechanistic identification of specific force coefficients for a general end mill. Int J Mach Tools Manuf 44(4):401–414
5. Wan M, Zhang WH, Qin GH, Tan G (2007) Efficient calibration of instantaneous cutting force coefficients and runout parameters for general end mills. Int J Mach Tools Manuf 47(11):1767–1776
6. Gonzalo O, Jauregi H, Uriarte LG, López De Lacalle LN (2009) Prediction of specific force coefficients from a FEM cutting model. Int J Adv Manuf Technol 43(3–4):348–356
7. Adetoro OB, Wen PH (2010) Prediction of mechanistic cutting force coefficients using ALE formulation. Int J Adv Manuf Technol 46(1–4):79–90
8. Adem KAM, Fales R, El-Gizawy AS (2015) Identification of cutting force coefficients for the linear and nonlinear force models in end milling process using average forces and optimization technique methods. Int J Adv Manuf Technol 79(9–12):1671–1687
9. Budak E, Altintas Y, Armarego E (1996) Prediction of milling force coefficients from orthogonal cutting data. J Manuf Sci Eng 118(2): 216–224
10. Oxley PLB, Young H (1989) The mechanics of machining: an analytical approach to assessing machinability. Ellis Horwood Publisher:136–182
11. Li HZ, Zhang WB, Li XP (2001) Modelling of cutting forces in helical end milling using a predictive machining theory. Int J Mech Sci 43(8):1711–1730
12. Lalwani DI, Mehta NK, Jain PK (2009) Extension of Oxley's predictive machining theory for Johnson and Cook flow stress model. J Mater Process Tech 209(12–13):5305–5312
13. Moufki A, Dudzinski D, Le Coz G (2015) Prediction of cutting forces from an analytical model of oblique cutting, application to peripheral milling of Ti 6Al 4V alloy. Int J Adv Manuf Technol 81(1–4):615–626
14. Fu Z, Yang W, Wang X, Leopold J (2015) An analytical force model for ball end milling based on a predictive machining theory considering cutter runout. Int J Adv Manuf Technol:1–12
15. Budak E, Kops L (2000) Improving productivity and part quality in milling of titanium based impellers by chatter suppression and force control. Cirp Ann-Manuf Techn 49(1):31–36
16. Budak E (2003) An analytical design method for milling cutters with nonconstant pitch to increase stability, part I: theory. J Manuf Sci Eng 125(1):29–34
17. Wan M, Zhang W, Dang J, Yang Y (2009) New procedures for calibration of instantaneous cutting force coefficients and cutter runout parameters in peripheral milling. Int J Mach Tools Manuf 49(14):1144–1151
18. Li B, Hu Y, Wang X, Li C, Li X (2011) An analytical model of oblique cutting with application to end milling. Mach Sci Technol 15(4):453–484
19. Moufki A, Dudzinski D, Molinari A, Rausch M (2000) Thermoviscoplastic modelling of oblique cutting: forces and chip flow predictions. Int J Mech Sci 42(6):1205–1232
20. Leopold J. Mechanical and physical models of machining: Proceedings of the 2th CIRP international workshop on modeling of machining operations, Nantes, France, 1999[C].
21. Li B, Wang X, Hu Y, Li C (2011) Analytical prediction of cutting forces in orthogonal cutting using unequal division shear zone model. Int J Adv Manuf Technol 54(5–8):431–443
22. Budak E, Ozlu E (2008) Development of a thermomechanical cutting process model for machining process simulations. Cirp Ann-Manuf Techn 57(1):97–100
23. Ozlu E, Budak E, Molinari A (2009) Analytical and experimental investigation of rake contact and friction behavior in metal cutting. Int J Mach Tools Manuf 49(11):865–875
24. Joshi SS, Melkote SN (2004) An explanation for the size effect in machining using strain gradient plasticity. J Manuf Sci Eng 126(4): 679–684

25. Ding H, Shen N, Shin YC (2011) Modeling of grain refinement in aluminum and copper subjected to cutting. Comput Mater Sci 50(10):3016–3025
26. Bissacco G, Hansen HN, Slunsky J (2008) Modelling the cutting edge radius size effect for force prediction in micro milling. CIRP Ann Manuf Technol 57(1):113–116
27. Abdelmoneim ME, Scrutton R (1974) Tool edge roundness and stable build-up formation in finish machining. J Manuf Sci Eng 96(4):1258–1267
28. Waldorf DJ, DeVor RE, Kapoor SG (1998) A slip-line field for ploughing during orthogonal cutting. Journal of Manufacturing Science and Engineering, Transactions of the ASME 120(4):693–699
29. Armarego E, Deshpande N (1993) Force prediction models and CAD/CAM software for helical tooth milling processes. II Peripheral milling operations Int J Prod Res 31(10):2319–2336
30. Zhang X, Xiong C, Ding Y.(2012) Dynamic cutter runout measurement with laser sensor. In:Intelligent Robotics and Applications. Springer Berlin Heidelberg, 264–272
31. Srinivasa YV, Shunmugam MS (2013) Mechanistic model for prediction of cutting forces in micro end-milling and experimental comparison. Int J Mach Tools Manuf 67:18–27
32. Diez Cifuentes E, Pérez García H, Guzmán Villaseñor M, Vizán Idoipe A (2010) Dynamic analysis of runout correction in milling. Int J Mach Tools Manuf 50(8):709–717